Experimental investigation of vortex-induced vibrations of a circular cylinder

Agathe Schmider, Franck Kerhervé, Laurent Cordier, Andreas Spohn, Nicolas Dellinger

12th International Symposium on Turbulence and Shear Flow Phenomena (TSFP12)
Osaka, Japan (Online), July 19-22, 2022

EXPERIMENTAL INVESTIGATION OF VORTEX-INDUCED VIBRATIONS OF A CIRCULAR CYLINDER

Agathe Schmider[1], F. Kerhervé[2], L. Cordier[3], A. Spohn[4], N. Dellinger[5]
Institut Pprime[1,2,3,4]/ICube[5]
Université de Poitiers[1,2]/ENSMA[4]/CNRS[3]/Université de Strasbourg[5]
agathe.schmider@univ-poitiers.fr

ABSTRACT

A new device to study flow-induced vibrations (FIV) under adjustable structural damping ratio is presented. In the presented work, an elastically-mounted cylinder is considered for validation in the context of vortex-induced vibrations (VIV). A DC motor is coupled to the oscillating mass and allows to simulate for positive or negative damping through forcing. When the forcing is appropriately settled to simulate a low structural damping ratio, the standard three-branch response for such system is well recovered and compare well with the literature. Inversely, when the forcing is settled to simulate high damping ratio, the two-branch response is also well reproduced. Flow velocity surveys obtained with Particle Image Velocimetry (PIV) are reported and show that the different VIV wake modes described in the literature are also well recovered by this new experimental device.

INTRODUCTION

Flow-induced vibrations (FIV) over elastically mounted bluff-bodies occur whenever a bluff body structure is immersed in a fluid stream. When vortex shedding frequency is close to the natural frequency of the bluff structure, large oscillations can occur and may result in potential damages. Such coupling is referred to as vortex-induced vibrations (VIVs). Most of the early research on FIVs and VIVs was mainly guided towards their suppression (Zdravkovich, 1981) in the context of avoiding engineering failures. Only recently, these large-scale oscillations were considered an opportunity for energy harvesting in rivers. The VIVACE converter designed by Bernitsas *et al.* (2008) is a typical arrangement with a circular cylinder mounted on linear springs and connected to a power generator. It demonstrated an efficiency comparable to other wind or marine energy devices.

The goal of the on-going work presented here is to improve the efficiency of a similar system thanks to controllable mechanical characteristics among which damping and stiffness. While former studies focus on arrangements with constant viscous damping, the present study takes advantage of an oscillator with adjustable characteristics. At this end, the present experimental set-up allows to change damping as a function of oscillation amplitude. In addition, the system stiffness can also be adapted to match the system resonance frequency to the vortex shedding frequency. The paper is organised as follows. The overall device is first described. Its validation in terms of vibration response is then discussed.

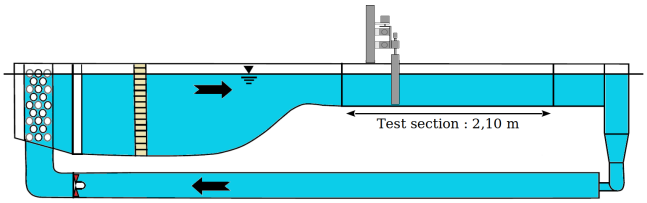

Figure 1. Simplified diagram of the water channel and position of the experimental arrangement

EXPERIMENTAL SET-UP

In preamble, the experimental set-up including the water channel, the VIV device and the instrumentation are presented.

Water channel

The experiments presented are conducted in the home-made circulating water channel Hydra III at Institut Pprime (Poitiers, France). The overall set-up is schematically represented in Figure 1. The flow is entreined by an axial pump located in the return flow of the closed circuit water channel. The test section is 2.1 m long, 0.51 m wide and 0.51 m height and is made of glass windows to allow optical access from both sides, as well from below. The water depth in the test section is fixed to 0.33 m. The freestream velocity ranges from 5 to 45 $\mathrm{cm\,s^{-1}}$. The flow uniformity all along the test section was checked in different planes by two-dimensional two-component (2D-2C) Particle Image Velocimetry (PIV). The measured deviation from flow uniformity of the velocity profiles is less than 1%. The measured flow unsteadiness is less than 5% in the whole range of velocities.

Experimental VIV device

The oscillating device is shown in Figure 2. A circular hollow cylinder made in aluminum of diameter $D = 50$ mm, length $L = 0.4$ m and thickness $e = 1.8$ mm is vertically immersed in the water channel. The blockage ratio due to the presence of the cylinder in the test section is 10%. A gap between the cylinder end and the channel floor is set to 2 mm. The cylinder is mounted on a platform made in aluminum which supports three OAV air bearings which are supplied by pressurized air at 4 bars. These air bearings guide the mobile platform with negligible mechanical friction in the crossflow direction along two shafts made in high precision stainless steel of 20 ± 0.02 mm diameter. A pair of linear springs (LeeSpings LE014B13S) mounted in parallel on each side furnish the restoring force. The resulting total stiffness coefficient is $k = 0.022\ \mathrm{N\,mm^{-1}}$. A low inertia 24V DC servo motor with a dual track encoder is coupled to the oscillating

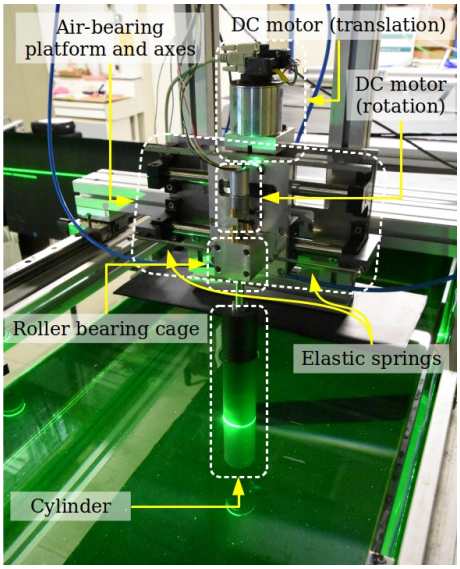

Figure 2. Experimental VIV device.

platform with a rack and pinion mechanism. Such arrangement results in additional dry friction due to the mechanical coupling. The motivations for such arrangement is threefold. First, it allows to measure in real-time accurately and robustly the position y and velocity $\dot{y}$ of the cylinder. Second, it allows to quantify the energy that can be harvested from the oscillating system by measuring on-line the generated current. Last, the motor can be used to move arbitrarily the cylinder or to simulate positive or negative damping effect, such as to compensate for the additional source of friction (see below), for instance.

With this arrangement, the cylinder can operate displacement over $\pm 2D$ in the cross-flow direction with minimal damping. The overall oscillating mass is $m = 2.486$ kg which results in a mass ratio $m^* = m/m_A = 3.8$ with m_A the displaced mass of water.

Instrumentation

The 24V DC motor is directly used to measure both the displacement y and velocity $\dot{y}$ of the cylinder. The in-built encoder provides TTL output signals with 500 pulses per revolution and enables to measure position and speed with a ± 0.15 mm accuracy. Both signals are sampled at 500 Hz with a NI PXIe-6356 I/O acquisition card. A planar two-component particle image velocimetry (PIV) system is used for velocity surveys in the near-wake of the cylinder. The PIV system includes a Nano L $50-50$ PIV laser from Litron Ltd (wavelength 532 nm) of 50 mJ per pulse and a Dantec SpeedSence 1040 camera with a resolution of 2320×1726 pixels. This camera is oriented towards the wake region, through a mirror inclined at 45° installed underneath the water channel. The measurement plane is located at mid-height of the water channel and covers a region of $8D \times 9D$ including the cylinder. The laser sheet is 1 mm thick. Polyamide particles of 50 µm diameter are used for flow seeding. The instantaneous vector fields are obtained using the acquisition software Davis 10 from Lavision. A dynamic mask following the cylinder displacement is used to avoid spurious correlations. The location of the mask for a given pair of images is set by the simultaneous measurements of the cylinder location. A conventional direct cross-correlation process including multipass windows (from 64×64 to 32×32) with 50% overlapping is used, leading to a final vector spacing of $0.09D$ in both directions. A bad-vector-replacement step is provided using a 5×5 median interpolation method. Finally, for a given PIV run, 3000 snapshots sampled at $f_{\mathrm{PIV}} = 15$ Hz, covering approximately 50 oscillations of the cylinder, are acquired.

DAMPING SIMULATION

The elastically-mounted cylinder behaves similarly to a one-degree of freedom damped oscillator under unsteady external forces, here hydrodynamic forces exerted by the vortical structures shed in the wake of the cylinder. The fluid-dynamic forces can be reduced to the lift force which may be represented by the unsteady lift coefficient $C_L(t)$. In addition, dry friction is also exerted on the oscillating mass due to the coupling of the oscillating platform with the DC motor. This additional force can be modelled as a Coulomb term of the form $F_f \mathrm{sign}(\dot{y})$ (Meirovitch, 1986) where F_f has to be evaluated. In the meantime, the DC motor can be driven such that an additional forcing is applied to the motion of the cylinder to compensate, for example, for dry friction or damping. This may be seen as a forcing of the cylinder displacement. The later can thus be modelled as,

$$m\ddot{y} + (c - \Delta_c)\dot{y} + (k - \Delta_k)y + (F_f - \Delta_f)\mathrm{sign}(\dot{y}) = \frac{1}{2}\rho U_\infty^2 D L C_L(t) \quad (1)$$

where the term $F_{DC}(\gamma, t) = \Delta_c \dot{y} + \Delta_k y + \Delta_f \mathrm{sign}(y)$, with $\gamma = [\Delta_c, \Delta_k, \Delta_f]^T$, accounts for the force exerted by the DC motor. The coefficient Δ_c can be fixed to positive or negative value when accounting for, respectively, reduction or addition of damping. Similarly, Δ_k accounts for simulating additional stiffness without modifying the linear springs. Note that in the present study this coefficient is set to zero. Finally, the value of Δ_f is here selected such that the dry friction is optimally compensated as it will be discussed in the following part. For a given triplet vector γ, the forcing law $F_{DC}(\gamma, t)$ is applied to the oscillating platform through the command in current of the DC motor in a closed-loop manner which gives in return a corresponding torque $\Gamma(t)$. At this end, a NI PXI-RT board (PXIe-1071) is connected to two NI PXIe-6356 I/O cards, one being used for the acquisition of signals only (among which y and $\dot{y}$) and one for the command of the DC motor.

FREE-DECAY TESTS FOR DRY FRICTION COMPENSATION

Free decay tests were first conducted in air and quiescent water to evaluate the structural damping natural frequencies of the VIV device. As a reference, the DC motor is first uncoupled from the oscillating platform so that no dry friction is exerted, i.e. that the plateform oscillates freely with negligible damping. This configuration is further referred as R_0 and is similar to that investigated by few authors among which Zhao *et al.* (2014); Khalak & Williamson (1997). As mentioned previously, while dry friction is added when the DC motor is coupled with the oscillating platform, this arrangement also allows different configuration to be tested depending on the value of the parameter vector γ. These configurations are further referred as C_{Δ_f, Δ_c} (Δ_k is here omitted as it is kept fixed to zero in the presented work). The case $C_{0,0}$ therefore denotes null

	Air			Water		
Case	k (N m^{-1})	c (N s m^{-1})	f_{na} (Hz)	f_{nw} (Hz)	ζ	$m^*\zeta$
R_0	0.022	0.071	0.0485	0.433	0.00424	0.016
$C_{0,0}$	0.022	1.19	0.463	0.419	0.0694	0.305
$C_{\Delta_f^*,0}$	0.022	0.328	0.459	0.0414	0.019	0.079

Table 1. Natural frequencies f_{na} (respectively f_{nw}) in air (respectively in water), structural damping ratio and structural mass-damping ratio for the three different arrangements.

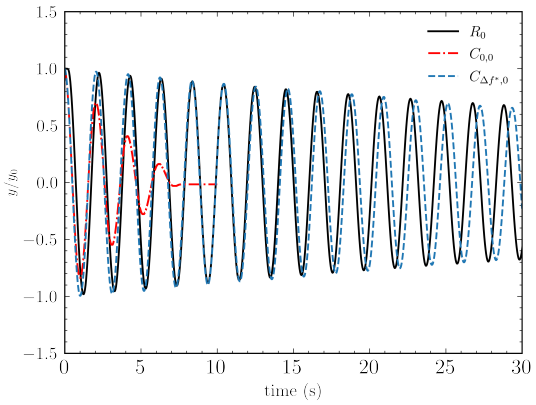

Figure 3. Time histories of the displacement of the cylinder for free-decay tests in air for the different arrangements.

compensation for dry friction and damping. The subscript Δ_f^* is further used as the value of Δ_f which allows for full compensation of the dry friction. When this parameter is properly set, the $C_{\Delta_f^*,0}$ arrangement is expected to behave similarly to the reference arrangement R_0.

Note that for the reference case, since the DC motor is uncoupled, measurement of the displacement of the cylinder can not be effected thanks to the encoder. Images sampled at a frequency of 20 Hz were therefore recorded thanks to the FLIR Grasshopper3 camera to track the cylinder and to extract its displacement over time. While not reported here, specific validation tests have been effected to compare the displacement obtained from optical tracking with the one obtained from the encoder.

Results obtained for the free-decay tests conducted in air for the R_0, $C_{0,0}$ and $C_{\Delta_f^*,0}$ arrangements are presented in Figure 3. The free-response of the different arrangements is that of a damped oscillator. When coupling the DC motor to the oscillating platform ($C_{0,0}$ configuration), the system response is, as expected, found to experience significant damping compared to the reference arrangement R_0. This is representative of higher structural damping for this arrangement. A first guess of the value of Δ_f^* which fully compensates for the dry friction is obtained following the work of Feeny & Liang (1996). Trial and error tests in air are then conducted to adjust Δ_f^* such that the free-decay responses of the R_0 and $C_{\Delta_f^*,0}$ properly matches. As shown in Figure 3, the selected value allows to recover almost perfectly the free-response of the free-friction reference case. The small discrepancies observed in the free-response as the time increases are believed to be due to small change in the mass of the mobile system due to the inertia of the DC motor itself. This results in a slight decrease of the natural frequency of the system while the structural damping is properly recovered. While not reported here for conciseness, similar trends are observed when the free decay tests are conducted in water. Values of the natural frequencies f_{na} and f_{nw} for the three arrangements found in air and still water respectively are summarised in Table 1. That of the structural damping ratio (defined only in still water) with consideration of the added mass and defined as $\zeta = cf_{na}/f_{nw}2\sqrt{km}$ are also reported. As a key parameter, the structural mass-damping ratio $m^*\zeta$ is also evaluated for the three arrangements. The $C_{0,0}$ case exhibits a high structural mass-damping ratio (an order of magnitude larger than that of the R_0 arrangement) due to the additional friction. In contrast, the free-damping R_0 and compensated dry-friction $C_{\Delta_f^*,0}$ cases are characterised by a low ratio. This suggests that the presented device can allow to simulate two- and three-branches VIV system's responses in a straightforward manner. At this stage, arrangements R_0 and $C_{\Delta^*,0}$ exhibit similar free-decay responses in air and still water and are therefore expected to provide similar vibration responses with regards to freestream velocity.

VIBRATING RESPONSES OF THE DIFFERENT ARRANGEMENTS

In this section, the amplitude and frequency responses of the different arrangements are investigated. The amplitude of the cylinder, hereafter A_{10}^*, is defined as the mean of the highest 10% of peak amplitude response normalised by the cylinder's diameter.

Reference arrangement & Model response

The amplitude response of the R_0 arrangement is illustrated in Figure 4(top) as a function of the reduced velocity $U^* = U_\infty/f_{nw}D$ and is compared against the results of Soti *et al.* (2018). Note that both arrangement have the same structural damping ratio ζ of approximatively 0.020. The reference arrangement R_0 exhibits a typical VIV amplitude response in three branches: (i) an initial branch for $U^* \leq 4.8$ with low oscillation amplitude, (ii) an upper branch lying in the range $4.8 \leq U^* \leq 6.6$ where the cylinder experiences largest amplitudes of oscillations of $\approx 0.8D$ and (iii) a lower branch within the range $6.6 \leq U^* \leq 9.5$ where A_{10} limits to $\approx 0.55D$. The region above $U^* = 9.5$ is generally referred as the desynchronised region and is characterised by very negligible oscillations. The normalised frequency response is shown in Figure 4(bottom) as black square symbols. The power spectral density (PSD) of the displacement for a given value of the reduced frequency has been evaluated and the frequency of the larger energy peak is extracted. Along the initial branch, the cylinder's frequency response equals the shedding frequency f_{sh} measured to be equal to $0.21U_\infty/D$. When moving towards the lower branch, the cylinder's frequency slightly increases

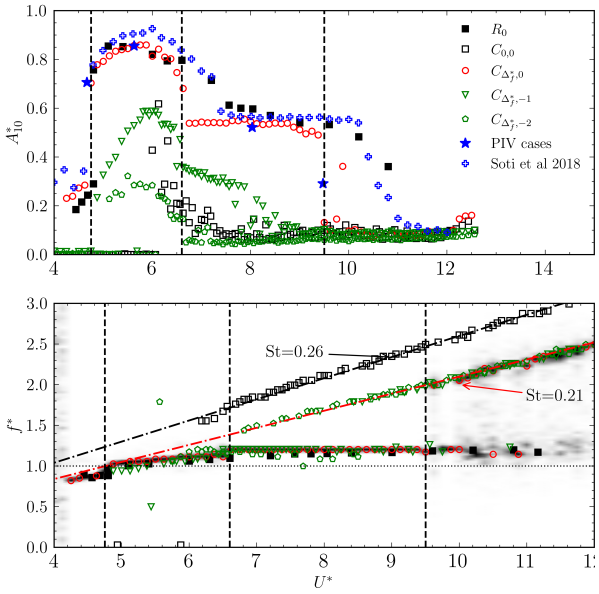

Figure 4. (a) Amplitude response A^* as function of the relative velocity U^* for the different arrangements compared by the results of Soti *et al.* (2018). (b) Frequency response as a function of the relative velocity U^* of the $C_{\Delta^*_f}$ configuration.

to lock approximatively in the natural system frequency f_{nw}. This is shown by the horizontal dashed line at $f^* = 1$. The frequency response along the upper and lower branches is said to be synchronised until it reaches the desynchronised region. For the later, the frequency response is found to reach again the shedding frequency while the vibration response may also experiences a low amplitude modulation at the natural frequency. In this region, the PSDs effectively exhibit two frequency peaks. These results are well consistent with that reported in the literature for low structural damping ratio $m^*\zeta$ (Khalak & Williamson, 1999; Zhao *et al.*, 2014) and suggest that the R_0 arrangement is properly designed and can be here considered as a reference case for what follows.

Effect of dry friction compensation

The $C_{0,0}$ arrangement is now examined. This arrangement has a high $m^*\zeta$ ratio and is consequently expected to experience a distinctly different response. The amplitude and frequency responses as a function of the reduced velocity are reported in Figure 4 as open squares. In contrast to the reference arrangement R_0, the range of reduced velocity where oscillations are observed for the $C_{0,0}$ case is limited only to $5 \leq U^* \leq 8$. The synchronisation regime is therefore found to be narrower. The upper limit of the oscillation amplitude is also lower with a peak value of about $0.55D$ comparable with the amplitude value obtained for the R_0 arrangement in the lower branch regime. The amplitude response is typical of a Feng-type response (Khalak & Williamson, 1999) where only the initial and lower branches exist. While not put clearly here in evidence for conciseness, an hysteretic transition also occurs between the two branches. The cylinder's frequency response equals the shedding frequency f_{sh} measured to be equal to $0.26U_\infty/D$ almost overall the two branches.

When introducing a correction for the dry friction in the form of a time-dependent torque, resulting in the $C_{\Delta^*_f,0}$ arrangement, the amplitude response now tends to match that of the reference arrangement as shown in Figure 4(top) by the open circles symbols. The difference in the structural damping ratio and in the mass of the moving system is believed to be responsible for the small discrepancies observed. A correction for the virtually added stiffness should also be addressed to perfectly recover the amplitude response of the reference arrangement. The three branches are however well properly recovered. Similar conclusion can be made with regards to the frequency response reported in Figure 4(bottom). The dominant frequency of the oscillating cylinder fully matches that observed for the reference arrangement. Even the modulated oscillations in the desyncrhonisation region ($U^* > 9.5$) observed for the R_O arrangement are recovered. The correction implemented for the added dry friction can therefore be considered as satisfactory.

It is noteworthy that when varying the coefficient Δ_c, different response regimes can be examined. This is illustrated again in Figure 4 where the results for the case $C_{xx,0}$ is reported as an illustration. Here, the value of Δ_c has been chosen to simulate energy extraction from the system. Adding some damping to the moving system results in a drop of the amplitude response while the frequency response remains almost unchanged as reported in Figure 4 by the green open symbols. The presented device therefore allows to simulate different VIV regimes between the typical low- and high- mass ratio typical responses.

VIV REGIMES

Since the frequency response of the oscillating cylinder is quasi-periodic (see Section **??**), the formation of the vortices in the cylinder wake is analyzed with a phase-averaged approach. In what follows, the phase-averaged velocity is defined according to the phase $\phi_i \in [0, 360°]$ $(i = 0\ldots, N_\phi)$ of the dominant oscillation period, where N_ϕ denotes the total number of phases considered. Due to a slight variation in time of the period of the dominant oscillation ($\pm 6\%$), the temporal position of a given phase changes slightly between two consecutive maxima. Therefore, the instants corresponding to a given phase ϕ_i are first evaluated independently for each oscillation period. For a given value ϕ_i, the PIV fields corresponding to the range $[\phi_i \pm \Delta\phi]$ are then collected and averaged to form the phase-averaged velocity fields $\overline{\boldsymbol{u}_i}$. The latter thus describes, on average, the velocity field obtained in the wake of the cylinder at a given phase instant of the VIV process. In the following, we consider $N_\phi = 12$ and $\Delta\phi = 10°$. The latter value has been found to present a good compromise between the phase localization and the number of PIV snapshots necessary to get a satisfactory statistical convergence. The obtained two-dimensional phase-averaged velocity field is then used to compute a phase-averaged vorticity field from which wake regimes can be identified.

Sequences of phase-averaged vorticity fields are reported in Figure 5 for four different regimes. The later are highlighted in Figure 4(top) by the full star symbols. In the sequences reported in Figure 5, the cylinder going from one of its extreme position to the other. Figure 5(a) refers to a VIV regime at the end of the initial branch ($U^* = 4.7$). Two streets of vortices of opposite sign are identified. A double-row pattern of vortices with a streamwise spacing of approximately $2D$ and a cross-flow spacing of approximatively $1.5D$ is observed. The initial branch is normally known to be associated with a $2S$ mode (two single vortex structures of opposite sign alternatively shed per oscillation cycle and concentrated along the wake center-line). The regime shown in Figure 5(a) exhibits

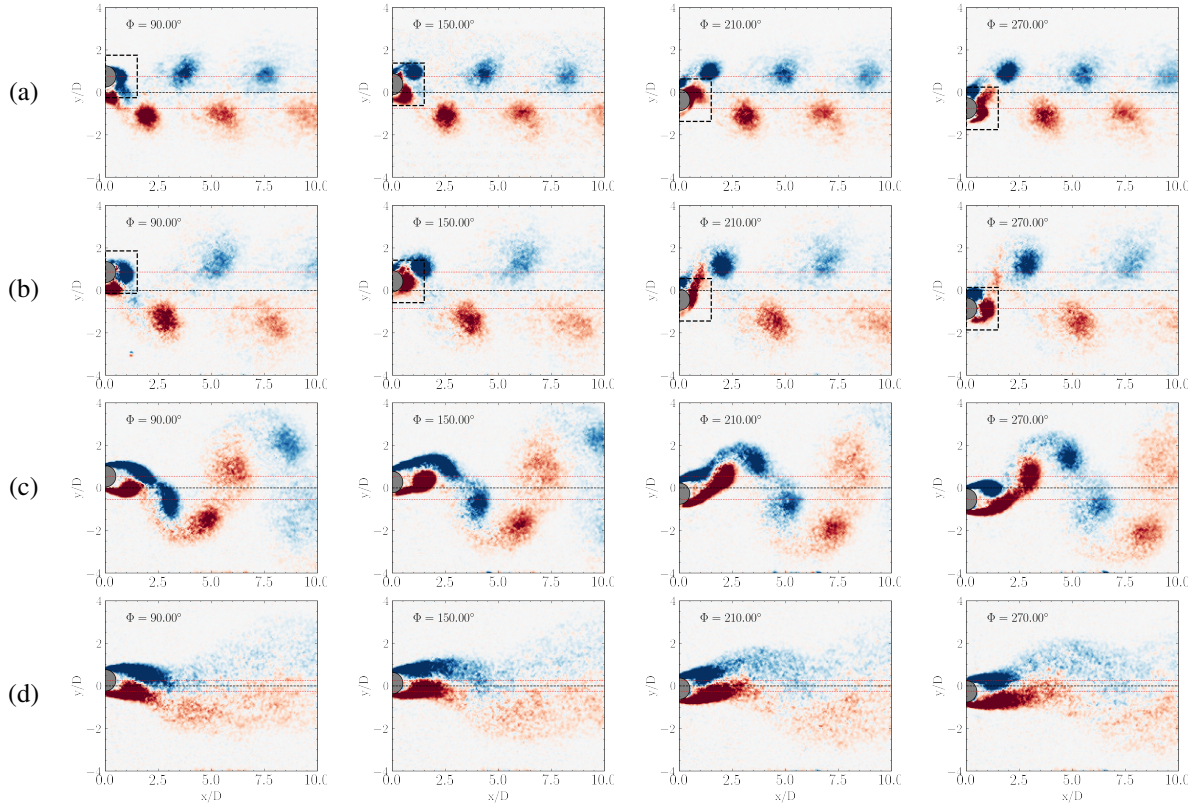

Figure 5. Sequences of phase-averaged vorticity snapshots for (a) $U^* = 4.5$, (b) $U^* = 5.6$, (c) $U^* = 8.0$ and (d) $U^* = 9.5$. Dry-friction compensated arrangement $C_{\Delta^*_f,0}$. The red dashed lines show the extremum location of the cylinder.

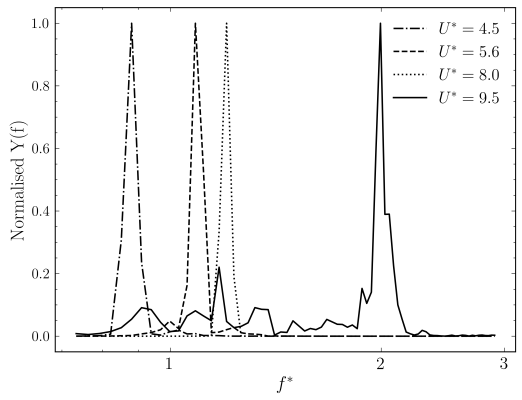

Figure 6. Power-spectral density (normalised by the maximum) of the cylinder's displacement for arrangement $C_{\Delta^*_f,0}$ at different reduced velocity U^*. The different regimes correspond to that shown in Figure 5

a transition from a $2S$ to a $2P$ mode observed along the upper and lower branches as shown in Figure 5(b)&(c) respectively. The $2P$ mode consists of two vortices of opposite sign shed per half oscillation cycle. The main difference observed in the wake pattern between the two latter figures, while associated to a similar $2P$ mode, is due to the rapid dissipation of the second vortex in the upper branch. Along the lower branch, the two vortices shed per oscillation cycle exhibit similar strength and therefore persists downstream as manifest in Figure 5(c). While in the lower branch the cylinder experience oscillation with amplitude lower than in the upper branch, it is noteworthy that the first vortex shed in the oscillation cycle is pushed further from the center-line due to the equivalent strength of the second vortex. In Figure 5(d), corresponding to the desynchronisation regime, the phase-averaged wake do not exhibit clear shedding vortical structures. It is noteworthy here that this regime is characterised by the coexistence of two dominant frequencies as discussed previously and as highlighted in Figure 6 where the power-spectral density of the cylinder's displacement is shown. The vorticity fields are here phase-averaged along the dominant frequency corresponding to the lock-in mechanism (first frequency peak) so that comparisons can be made with the other regimes. However, the vortex shedding occurs at the highest dominant frequency (second frequency peak). Phase-averaging along this second frequency peak would be required to better visualise the vortex shedding.

CONCLUSION

A new device for an elastically mounted cylinder experiencing vortex-induced vibrations (VIV) with adjustable damping and stiffness coefficients is presented. The change of these coefficients is simulated thanks to the coupling of a DC motor whose action on the oscillating mass can be modelled as a Coulomb term. Tests conducted show that the oscillating device allows to reproduce vibration regimes ranging from low- to high-mass ratio device configurations with vibrating responses similar to that typically reported in the literature. One main advantage of the proposed solution is that is is mechanically non-intrusive. Particle Image Velocimetry surveys performed in the wake of the cylinder for different VIV regimes are reported and shows that the different vortex modes well-documented in the literature are properly recovered.

ACKNOWLEDGMENTS

The current project was funded by Région Nouvelle-Aquitaine under the project NAQ Maggie 2018-1R10223.

REFERENCES

Bernitsas, MM, Raghavan, K, Ben-Simon, Y & Garcia, EMH 2008 Vivace (vortex induced vibration aquatic clean energy): A new concept in generation of clean and renewable energy from fluid flow. *Journal of offshore mechanics and Arctic engineering* **130** (4).

Feeny, BF & Liang, JW 1996 A decrement method for the simultaneous estimation of coulomb and viscous friction.

Khalak, Asif & Williamson, Charles HK 1997 Investigation of relative effects of mass and damping in vortex-induced vibration of a circular cylinder. *Journal of Wind Engineering and Industrial Aerodynamics* **69**, 341–350.

Khalak, Asif & Williamson, Charles HK 1999 Motions, forces and mode transitions in vortex-induced vibrations at low mass-damping. *Journal of fluids and Structures* **13** (7-8), 813–851.

Meirovitch, Leornard 1986 *Elements of Vibration Analysis*, 2nd edn. McGraw-Hill.

Soti, Atul Kumar, Zhao, Jisheng, Thompson, Mark C, Sheridan, John & Bhardwaj, Rajneesh 2018 Damping effects on vortex-induced vibration of a circular cylinder and implications for power extraction. *Journal of Fluids and Structures* **81**, 289–308.

Zdravkovich, MM 1981 Review and classification of various aerodynamic and hydrodynamic means for suppressing vortex shedding. *Journal of Wind Engineering and Industrial Aerodynamics* **7** (2), 145–189.

Zhao, J., Leontini, J. S., Lo Jacono, D. & Sheridan, J. 2014 Chaotic vortex induced vibrations. *Physics of Fluids* **26** (12).